Plasma Physics and
Controlled Fusion

PURPOSE-LED
PUBLISHING™

PAPER • **OPEN ACCESS**

Measurements of radial neutral density profiles from Balmer-α emission in Wendelstein 7-X

To cite this article: T Romba *et al* 2025 *Plasma Phys. Control. Fusion* **67** 055045

View the article online for updates and enhancements.

You may also like

- Turbulence-reduced high-performance scenarios in Wendelstein 7-X
O.P. Ford, M. Beurskens, S.A. Bozhenkov et al.

- Evaluation and validation of radial impurity density profiles from CXRS using neutral beam modelling in W7-X
T Romba, F Reimold, R J E Jaspers et al.

- 2D measurements of parallel counter-streaming flows in the W7-X scrape-off layer for attached and detached plasmas
V. Perseo, V. Winters, Y. Feng et al.

This content was downloaded from IP address 87.166.63.24 on 15/05/2025 at 16:05

OPEN ACCESS
IOP Publishing
Plasma Physics and Controlled Fusion

Plasma Phys. Control. Fusion **67** (2025) 055045 (9pp) https://doi.org/10.1088/1361-6587/add375

Measurements of radial neutral density profiles from Balmer-α emission in Wendelstein 7-X

T Romba[1,*], F Reimold[1], O P Ford[1], T W C Neelis[2], P Zs Poloskei[1] and the W7-X Team[3]

[1] Max Planck Institute for Plasma Physics, 17491 Greifswald, Germany
[2] Eindhoven University of Technology, 5612 AZ Eindhoven, The Netherlands

E-mail: thilo.romba@ipp.mpg.de

Received 9 January 2025, revised 23 April 2025
Accepted for publication 2 May 2025
Published 15 May 2025

Abstract

Radial neutral density profiles are estimated from measurements of passive H_α emission in the Wendelstein 7-X stellarator. To parametrize the generally three-dimensional distribution with a low number of degrees of freedom, the neutral density is reduced to a flux surface quantity. Accounting for emission from excitation and recombination processes, neutral density profiles are derived independently for each of the available lines of sight. Density profiles obtained from the different viewing geometries are found to vary within one order of magnitude. Toroidally oriented lines of sight predict systematically lower neutral densities when compared to poloidally oriented ones. This discrepancy is attributed to the simplifications inherent in the imposed model and significant differences in integration volumes across the viewing geometries. In line with expectations, obtained neutral densities are found to decrease with increasing plasma density. Key restrictions of the model include the reduction of the neutral density to a flux surface quantity, uncertainties in the plasma profiles and instrument function, and line integration effects outside the last closed flux surface.

Keywords: Wendelstein 7-X, neutral density, stellarator

1. Introduction

The population of neutrals within the confined plasma region has a strong influence on all transport channels in the plasma. The main effect of a neutral population on the energy confinement is given by enhancing radial energy transport via charge exchange (CX) reactions [1]. Similarly, CX reactions increase the radial transport of main ions. In addition, a finite population of neutrals inside the last closed flux surface (LCFS) may constitute a significant particle source by means of electron or ion impact ionization. In view of transport of impurities, CX reactions with background neutrals locally skew the ionization balance toward lower charge states [2].

Despite the significant influences on the power and particle balance, neutral densities in the confined region are typically simulated rather than measured [3, 4]. Although such measurements are possible spectroscopically, this is made difficult by the interplay of various effects.

As a consequence of the low local densities, emission signals from neutral hydrogen in the confined region are low. In

---

[3] See Grulke *et al* (https://doi.org/10.1088/1741-4326/ad2f4d) for the W7-X Team.
[*] Author to whom any correspondence should be addressed.

Original Content from this work may be used under the terms of the Creative Commons Attribution 4.0 licence. Any further distribution of this work must maintain attribution to the author(s) and the title of the work, journal citation and DOI.

© 2025 The Author(s). Published by IOP Publishing Ltd

combination with a component originating from the plasma edge, orders of magnitude brighter, a high dynamic range and high signal-to-noise ratio measurement is required. As neutral particles are not bound to the magnetic field, the neutral density is not a flux surface constant function, making it multidimensional. This high dimensionality causes the interpretation of signals to be highly complicated, calling for significant simplifications when interpreting the measured signals.

Based on the assumption of the neutral density being constant on flux surfaces, Goto *et al* [5] showed the feasibility of an assessment of radial neutral density profiles using passive H_α emission in the three-dimensional magnetic field of the Large Helical Device. The analysis was further refined by Fujii *et al* [6, 7], accounting for the transport of neutrals between subsequent CX reactions.

Here, we present the application of a spectroscopy-based assessment of radial neutral density profiles from H_α emission in the case of the optimized stellarator Wendelstein 7-X (W7-X) [8, 9]. Following Goto *et al* [5], the neutral density is assumed to be constant on a given flux surface, not accounting for transport effects between CX reactions. Section 2 introduces the underlying theory and the experimental approach. Section 3 discusses the numerical implementation and specifics to the W7-X spectroscopy system. Neutral density profiles in case of a plasma density scan are discussed in section 4.

2. Methods

In order to infer the local properties of the neutral density population, typically line emission, encoding the local plasma properties, is spectroscopically assessed. In case of hydrogen plasmas, the Balmer-series transitions in the visible wavelength range are used. Besides good signal levels, this wavelength range enables access with standard spectrometer setups. In the following, the H_α transition ($n = 3 \rightarrow 2$) at 656.28 nm is assessed. It is the brightest transition of the Balmer series due to the low states, n, involved. A bright transition is necessary because as we approach fusion-relevant conditions, high ionization cross sections lead to lower and lower neutral densities in the confined region. The low densities subsequently give rise to faint signals from the hot plasma region.

Due to the efficient coupling of impurity, ion, and neutral temperatures via CX reactions [10], $T_0(\rho) = T_\mathrm{i}(\rho) = T_z(\rho)$ is assumed in the following. The radiative contributions from the various radial positions can then be disentangled through the local Doppler width of the emission. At a temperature T_0, a mass m, and radiation at the rest-wavelength λ_0, the Doppler width, σ of the radiation is given by:

$$\sigma = \lambda_0 \sqrt{\frac{\mathrm{e}T_0}{mc^2}}, \tag{1}$$

where c denotes the speed of light.

Caused by the scaling of σ with T_0, H_α emission from the hot core depicts a broad emission feature, dominantly contributing to the wings of any measured signal. In contrast, cold emission from the plasma edge only emits close to the rest wavelength at 656.28 nm. Due to the high density of neutrals near the plasma edge, the latter dominates the signal.

Due to the confining magnetic field, H_α emission experiences a broadening from the Zeeman effect. This broadened emission will be contributing measurably only to emission features with a few eV apparent temperature. This low-temperature central line contribution is anyway neglected in our neutral density profile estimation which focuses on the confined region.

Due to the emission being non-localized, the measured signal is of line integrated character. The measured intensity, $I_{H_\alpha}(\lambda)$, along a given line of sight (LoS) can be expressed as follows:

$$I_{H_\alpha}(\lambda) = \int_{\mathrm{LoS}} n_\mathrm{e}(l) \cdot \Bigg(\underbrace{n_0(l) \cdot \mathrm{PEC}^{\mathrm{exc}}_{3\rightarrow 2}}_{\text{excitation}} + \underbrace{n_\mathrm{i}(l) \cdot \mathrm{PEC}^{\mathrm{rec}}_{3\rightarrow 2}}_{\text{recombination}} \Bigg) \cdot \frac{1}{\sqrt{\pi \sigma^2_{H_\alpha}}} \exp\left[-\frac{(\lambda - \lambda_{H_\alpha})^2}{\sigma^2_{H_\alpha}} \right] \mathrm{d}l, \tag{2}$$

where $n_\mathrm{e}(l)$, $n_\mathrm{i}(l)$, and $n_0(l)$ denote the electron, ion, and neutral densities at location l, respectively. Local photon emissivity coefficients for excitation, $\mathrm{PEC}^{\mathrm{exc}}_{3\rightarrow 2}$, and recombination, $\mathrm{PEC}^{\mathrm{rec}}_{3\rightarrow 2}$, depend on the local plasma parameters and are given by adf15 coefficients from the OPEN-ADAS database [11]. Emission from CX reactions is omitted as it may only contribute significantly at higher temperatures. Photonic emission from molecular hydrogen is not explicitly accounted for but through the excitation component of equation (2). As uncertainties in the plasma parameters outside the confined region are large, inferred neutral densities outside the confined region are meaningless. This allows the neutral density outside the LCFS to also account for molecular emission via the excitation term of equation (2) in the form of an increase in local neutral density. Finally, radiation from impurities is not accounted for, as the region around H_α is free of impurity lines, with the closest transition being at 657.805 nm from CII, which falls outside the wavelength region assessed in the following.

The localization of emission via the local ion temperature underlying equation (2) is distorted by transport of neutrals between CX reactions. This distortion arises from the equilibration of a neutral's temperature with the local ion temperature being limited to instances of CX with background ions. Between these, neutrals travel independently of magnetic geometry. Thus, they potentially reach a flux surface b of temperature $T_{\mathrm{i},b}$ while maintaining temperature $T_{0,a}$, representative of flux surface a, the surface of the last CX reaction. If the neutral gets excited in its new location, photons representative of temperature $T_{0,a}$ are emitted from a location associated with temperature $T_{\mathrm{i},b}$, distorting the localization of the H_α emission via the local ion temperature.

The significance of this effect can be estimated based on the mean free path of the neutrals. It was found to be of the order of a few cm for comparable plasma parameters in the case of the large helical device [5]. Due to the uncertainties in the here determined neutral densities being large and plasmas in W7-X typically having a minor radius of around 50 cm, this effect is not accounted for in the following analysis. Note that a method to account for such transport effects has been proposed by Fujii *et al* [6, 7]. The implementation of this technique in the W7-X case is envisioned for future work.

Due to the Doppler width depending on T_i and reaction rates depending on n_e and T_e, the main plasma profiles need to be known in advance. Electron density and temperature profiles are measured by the Thomson scattering system of W7-X [12]. Ion temperature profiles are determined from CX recombination spectroscopy [13]. The n_i profiles for the recombination emission are derived from the measured n_e profiles assuming a radially constant effective plasma charge Z_eff derived from visible bremsstrahlung [14].

3. Implementation

The neutral density along the respective LoS constitutes the only unknown parameter in equation (2). Due to its three-dimensional characteristic in W7-X [3], the information of the available finite set of lines of sight is insufficient to resolve the multi-dimensional distribution, calling for a reduction in complexity. The necessary assumptions and simplifications in the analysis approach imposed for W7-X are discussed in the following.

3.1. Radial discretization

Due to the line integrated character of the H_α emission described by equation (2), the full path of a given LoS through the plasma volume needs to be traced. To illustrate, figure 1 depicts the LoS penetration depth for two sets of lines of sight of the W7-X CXRS system. The geometry is given in figure 2 and discussed in section 3.2. The length along the LoS is plotted on the abscissa while the local radial penetration depth in ρ is given on the ordinate. The underlying plasma equilibrium was calculated using the VMEC code [15]. The normalized minor radius of the plasma ρ relates to the normalized toroidal flux as calculated by VMEC like $\rho = \sqrt{s}$. Note that this approach introduces the assumption that neutral densities can be approximated as flux surface constants by use of the normalized radial coordinate.

The three-dimensional structure of the W7-X equilibrium and its complicating influences on the LoS integration paths is apparent by the complex penetration depth curves of figure 1. By introducing the normalized radial coordinate ρ, the LoS integration of equation (2) can be replaced by a summation. To do so, the penetration depth is discretized into radial bins of width $\Delta\rho$. Within each bin, plasma parameters are assumed constant, and the summation weight Δl is given by the sum of the path length of the LoS through the respective bins.

As previously discussed, the dominant H_α emission originates outside the confined plasma region due to the high local neutral densities. In this region, various aspects impede any deduction of a meaningful neutral density however. Besides VMEC being restricted to the confined region, a localization of the emission via T_i is impossible as Doppler width and instrument function width become comparable. These, together with poorly diagnosed plasma parameters with strong spatial gradients in the magnetic island region of W7-X, make a proper assessment of the neutral density outside the LCFS impossible with the available tools.

Although this component is not of interest here, it needs to be included in the fitting to some degree as the wings of this component extend into the spectral region that is of interest due to the instrument function (see section 3.3). In context of the introduced scheme, reasonable results are obtained when expanding the temperature profiles to $\rho = 1.2$ using an exponential decay from the temperature at $\rho = 1.0$ to 1 eV. Bin weights outside the LCFS are assumed to be the same as for the last bin inside the LCFS. The radial discretization is performed with a bin width of $\Delta\rho = 0.01$, giving rise to a total of 120 radial bins.

3.2. Spectroscopic system

To facilitate a spectroscopic analysis of the H_α emission given the previously discussed restrictions, a high fidelity spectrometer with a good signal-to-noise ratio is needed. To be sensitive to the faint core radiation, given the dominant cold edge component, a high dynamic range is necessary. At W7-X, the spectroscopic system routinely used for the analysis of the beam emission signal [13] fulfills these requirements. An overview of the system's geometry is given in figure 2.

This diagnostic measures the H_α spectrum for a total of 54 lines of sight using a spectrometer designed for operation at ITER [16]. The lines of sight are grouped into four fans covering the plasma under different incident angles. One fan is directed in the toroidal direction (AEA21_A), two fans hit the plasma under a 45° angle coming from the top of the vessel (AEM21), while the fourth fan crosses the plasma under an 45° angle coming from below the plasma (AET21, compare figure 2). The temporal resolution of the system is 10 ms under normal operating conditions.

3.3. Instrument function

With temperatures of the emission as low as 1 eV at the very plasma edge, the width of the edge emission is not governed by the Doppler width of equation (1) but rather the spreading of the radiation on the sensor by the instrument function. The instrument function of the spectrometer in use was measured at three different wavelengths using Neon pencil lamps [13], exhibiting an apparent temperature of around 5 eV. The low signal of the high-temperature wings of the spectrum demands for a sophisticated assessment of the instrument function introduced in the following.

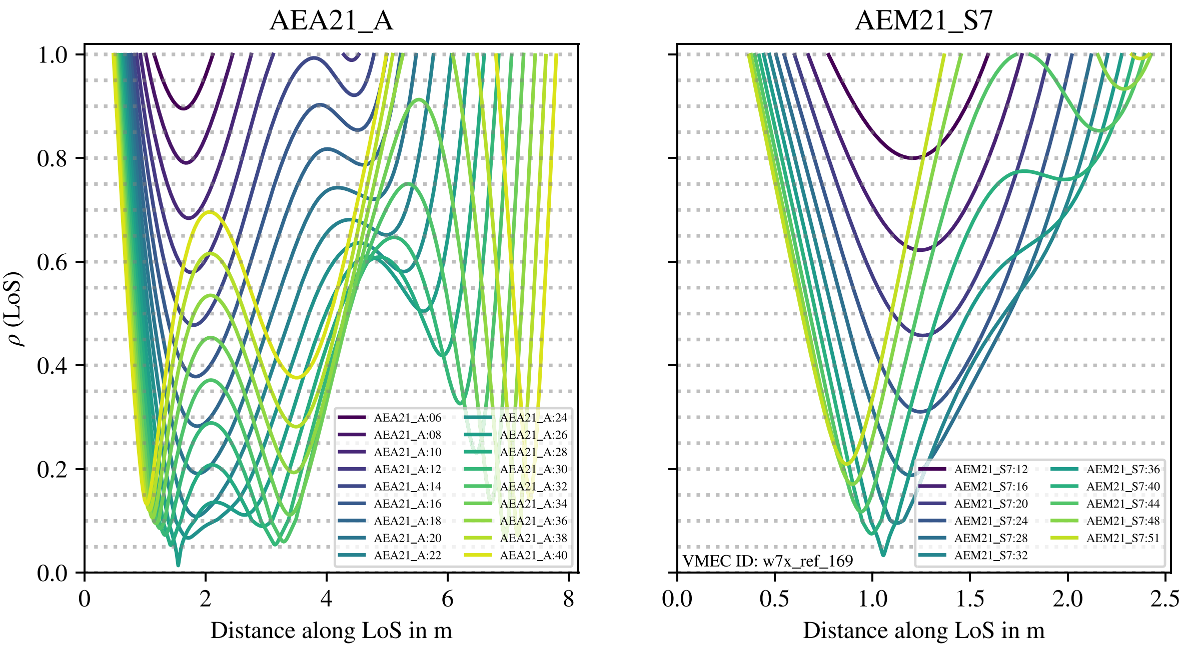

Figure 1. Penetration depth for toroidally (left) and poloidally (right) oriented lines of sight. Every fifth bin used for the radial discretization is indicated by a dashed horizontal line. The line of sight geometry is given in figure 2.

Figure 3 displays the instrument function at the three wavelengths as measured by the pencil lamp on a logarithmic scale in black. Diffraction peaks of the instrument function at up to 1 nm from the transition wavelength are observed. This causes emission of the low temperature component also to be present in the wings of the measured hydrogen spectrum. This effect causes a higher sensitivity of any fit towards the low-temperature component. This in turn significantly reduces the sensitivity of the fit to the high temperature components.

In addition to differences in the intensities of the three instrument functions in figure 3 caused by different emission rates of the neon transitions, differences in diffractive features are apparent. These differences indicate a wavelength dependence of the instrument function, making the estimation of an instrument function in the region of the H_α emission necessary. The instrument function at H_α, $\mathscr{F}_{H_\alpha}$, (green line in figure 3) relates to a synthetic one calculated from the linear combination of the transitions at 650.65 nm and 659.89 nm following:

$$\begin{aligned}\mathscr{F}_{H_\alpha} = {} & \frac{\lambda_{H_\alpha} - 650.65\,\mathrm{nm}}{659.89\,\mathrm{nm} - 650.65\,\mathrm{nm}} \cdot \mathscr{F}_{659.89\,\mathrm{nm}} \\ & + \frac{659.89\,\mathrm{nm} - \lambda_{H_\alpha}}{659.89\,\mathrm{nm} - 650.65\,\mathrm{nm}} \cdot \mathscr{F}_{650.65\,\mathrm{nm}}.\end{aligned} \qquad (3)$$

This linear combination is found to reproduce the emission at 653 nm well, hinting toward the validity of this approach. The radiative background is subtracted using a second order polynomial (orange curve in figure 3), ignoring the wavelength regions of the Neon transitions. The obtained instrument function at the H_α transition is normalized and convolved with the calculated plasma emission spectra. Due to diffractive effects observed across the camera chip, instrument functions are individually assessed and calculated for each available LoS.

3.4. Fitting of the H_α emission profile

Following the previous steps, the plasma emission as measured by the spectrometer for a given radial profile $n_0(\rho)$ can be calculated. In order to infer the experimental neutral density profile from comparison of measured and calculated spectra, it needs to be parameterized using a low number of degrees of freedom.

In the following, the neutral density profile is parameterized by a low number of non-radially equidistant spline nodes. Based on those, a full neutral density profile is obtained via cubic interpolation in logarithmic space. Nodes are more densely packed towards the plasma edge, the region where the largest gradients in the neutral density are expected. Neutral density profiles are inferred by performing a least-square fit of the calculated intensity of equation (2) to measured spectra. Each LoS is assessed individually to assess the validity of the assumption of flux surface constancy of the determined neutral density profiles. Imposing a joint fit across all measured spectra using a joint underlying neutral density profile did not yield sensible results.

As an additional constraint, locally peaked profiles of n_0 are penalized as simulations predict monotonously decreasing profiles [3]. To enforce this penalty, the least square residual is complemented by an additional error term. This error is zero in the case of hollow profiles and proportional to the maximal negative slope in the case of non-monotonous profiles. Note that the theoretical prediction of hollow n_0 profiles matches

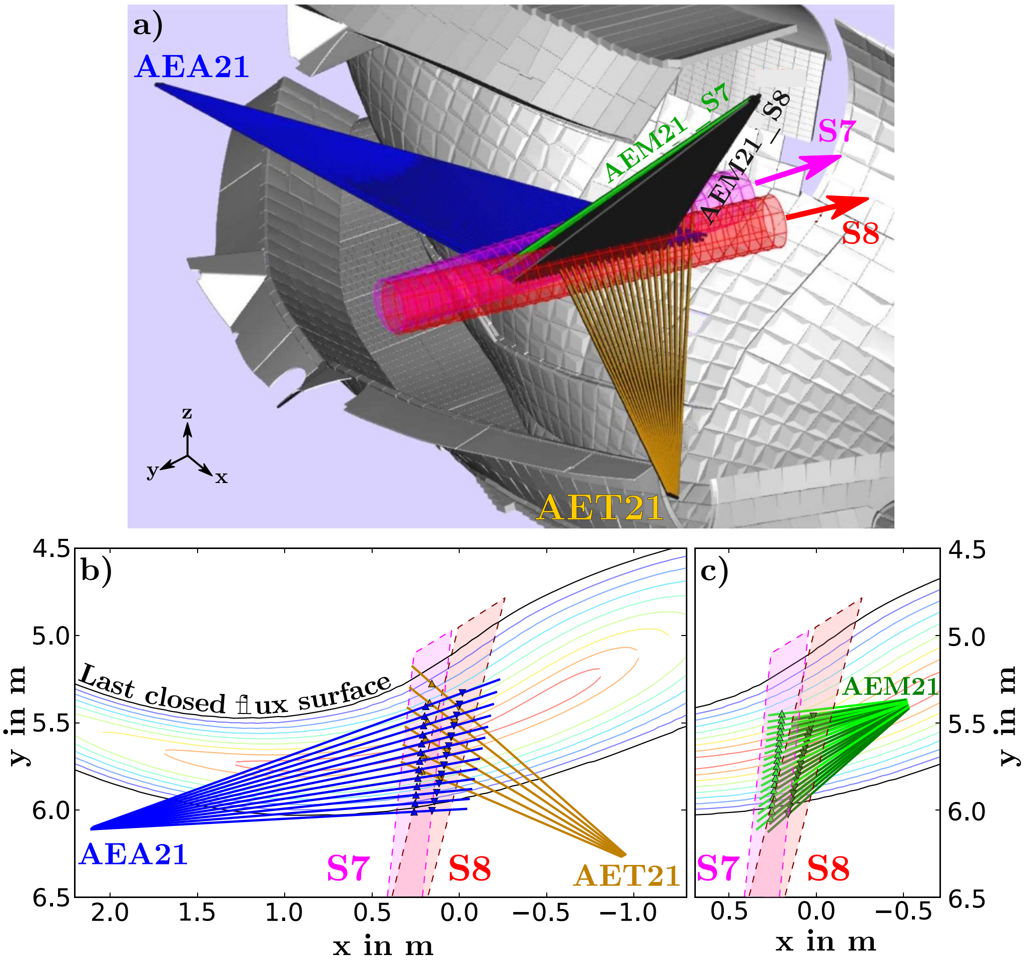

Figure 2. Line of sight geometry of the W7-X charge exchange recombination spectroscopy system used for the measurements of the assessed H_α emission. A three-dimensional view of the system, oriented around neutral beams S7 and S8, is given in panel (a). Panel (b) shows the projection of the toroidal AEA21 and poloidal AET21 line of sight arrays to a horizontal plane crossing the beam axes. Flux surfaces are indicated by lines following a color gradient. Likewise, panel (c) shows a projection of the poloidally oriented AEM21_S7 and AEM21_S8 line of sight arrays.

the naive expectation of a decreasing neutral density population with increasing T_i. Not imposing this constraint leads to a nonphysical increase of neutral density in the core region of the plasma, in turn indicative of the low sensitivity of the fit to hot temperature regions.

A measured spectrum with its fitted spectrum for the LoS of figure 3 for W7-X discharge 20180920.017 is given in figure 4. The plasma is heated by 4.5 MW of electron cyclotron resonant heating at an on-axis density of $6.0\times10^{19}\,\mathrm{m}^{-3}$. On-axis electron and ion temperatures are 3.0 keV and 1.6 keV, respectively, with around 30% of power being radiated. Spectra are averaged over a steady state window of 300 ms length starting at 4.2 s.

The goodness of a fit is assessed based on the relative residual between measurement, I_meas, and fit, I_calc, given by $(I_\mathrm{meas}-I_\mathrm{calc})/I_\mathrm{meas}$ indicated at the bottom of figure 4. A fit is identified as successful if the mean of the absolute relative residual and the standard deviation of the relative residual are below 0.15. Within figure 4, these limitations are indicated by the orange shaded region. As success of fits is found to strongly depend on the initial guess in the least-square fitting routine in use, failed fits are repeated with different initial guesses. Outside of the depicted region, the spectrum is dominated by noise. For edge-focused LoS, the detector is found to be saturated in the proximity of the H_α transition. To deal with saturated data points, their statistical weight is set to zero.

A mismatch of the fit with respect to the experimental data is observed in the far wings of the measured emission. These local emission peaks cannot be caused by hot emission but are a feature of the system's instrument function. Besides indications of inaccuracies in the interpolated instrument function, this reduces the method's sensitivity to neutral densities in high temperatures regions. Based on the shaded regions indicated in figure 4, this low sensitivity is expected to apply to densities inside half radius. As neutral densities in these regions are orders of magnitude too small to

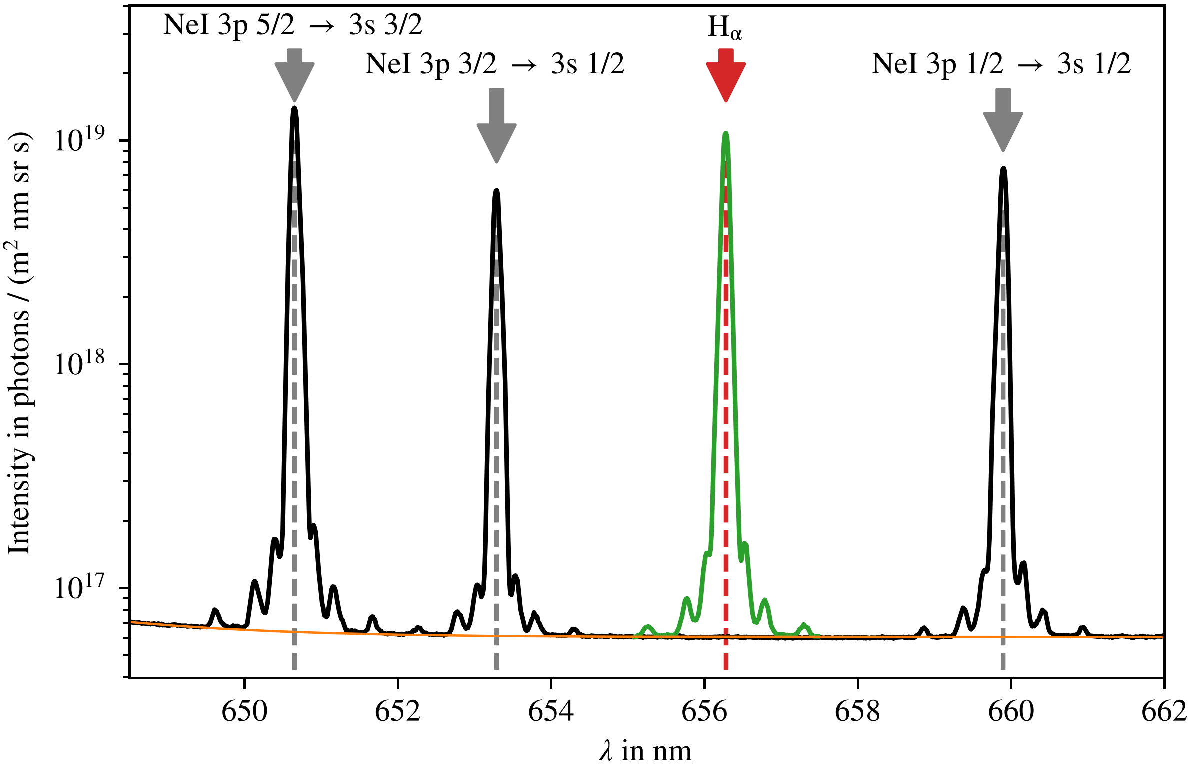

Figure 3. Instrument response measured for LoS AEA21_A:24 at three NeI transitions (black) with a synthetically calculated instrument function at H_α (green). The fitted background signal is given by the orange line; respective transition wavelengths are indicated by vertical dashed lines, neon transitions are labelled.

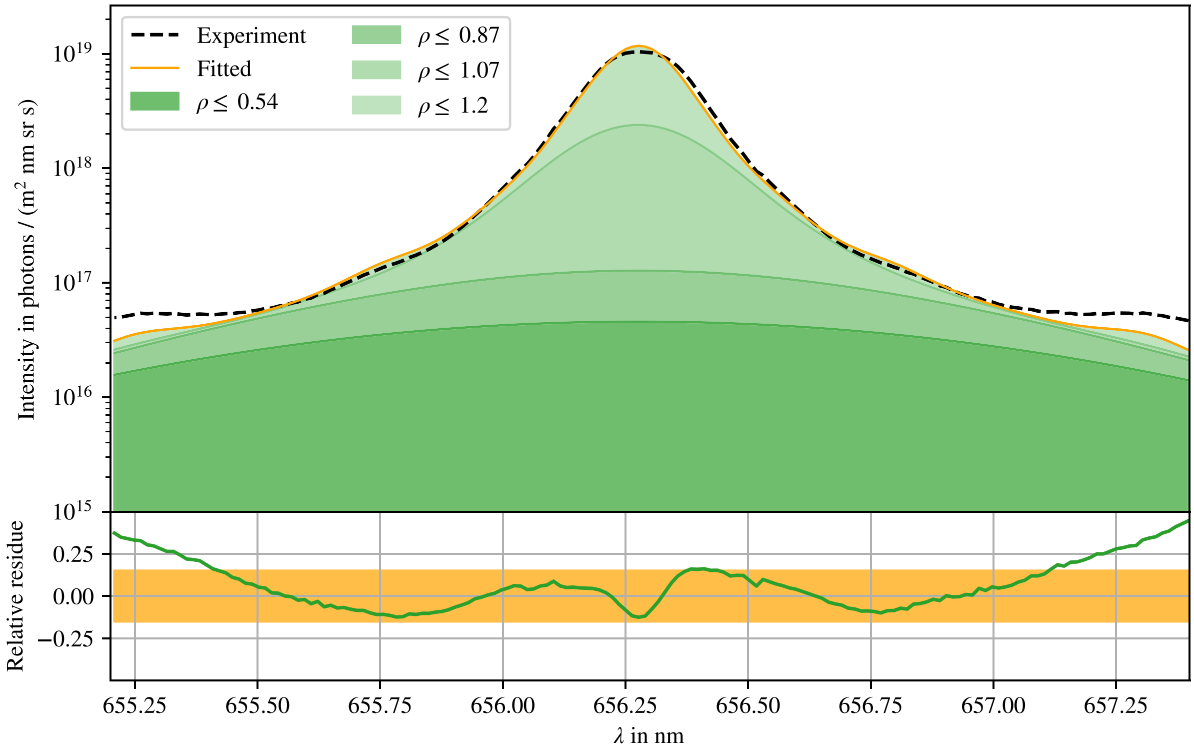

Figure 4. Measured (black) and fitted (orange) H_α spectra for the toroidally oriented line of sight AEA21_A:24. Contributions from different ρ are grouped into differently shaded regions, listed ρ values correspond to the spline knot locations in use. The relative residue is given by $(I_{\text{meas}} - I_{\text{calc}})/I_{\text{meas}}$, the orange shaded region mark the area of the relative residue below 0.15, used to assess the goodness of the fit.

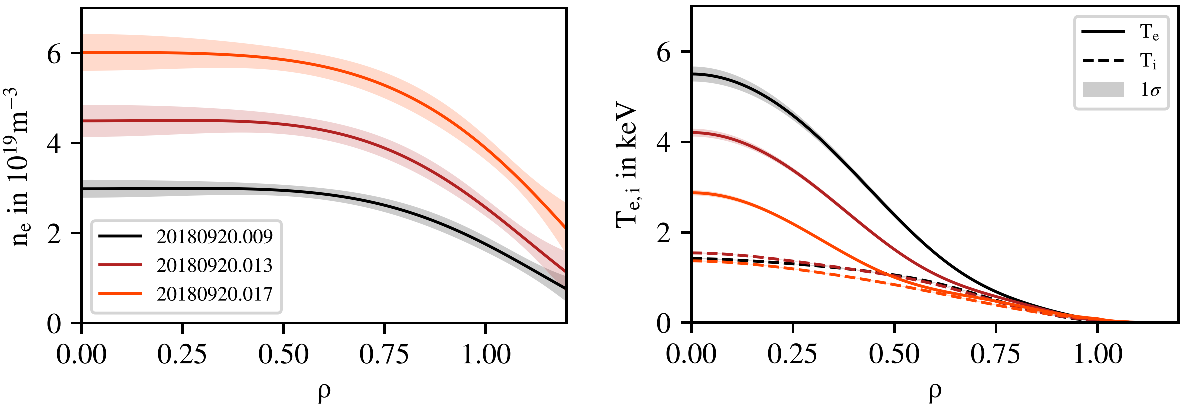

(a) Electron density profiles.

(b) Electron and ion temperature profiles.

Figure 5. Plasma profiles in the case of W7-X discharges 20 180920.009, .013, and .017, $t = 4.0-4.3$ s. The time window is slightly shifted relative to the one used for the neutral density analysis to contain a charge exchange blip at $t = 4.1$ s. Electron properties are measured by Thomson scattering [12], ion temperatures using charge exchange recombination spectroscopy [13].

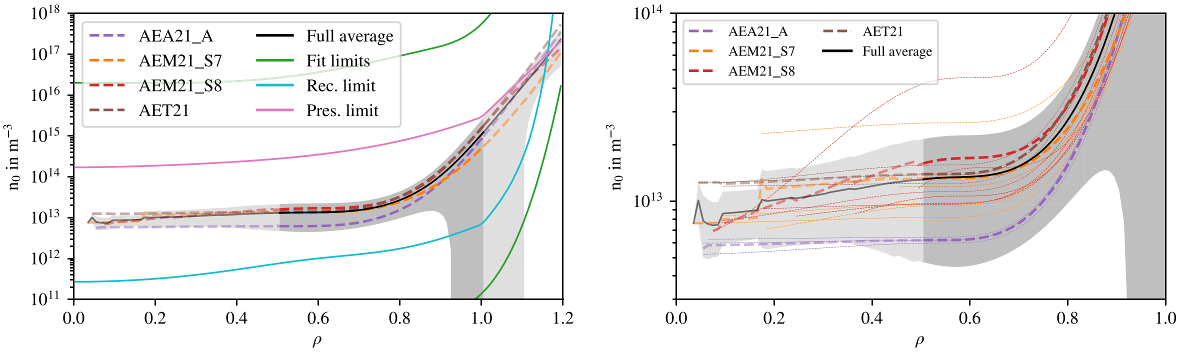

(a) Inferred neutral density profile with uncertainties and limits

(b) Zoom into the confined region and individual chord results

Figure 6. Obtained neutral density profiles in case of W7-X discharge 20 180920.017, $t = 4.2–4.5$ s. Results from the different line of sight arrays are color-coded, the average density of all LoS is given by a solid black line, its standard deviation is indicated by the gray shadowed region. Averaged densities of individual arrays are given by dashed lines in the respective color. Fitting boundaries of n_0 are indicated by green lines, regions of low sensitivity of the method are grayed out. An upper limit for the density based on constant neutral pressure (pink) and a lower limit based on the equilibrium of ionization and recombination (cyan) complement the figure.

significantly affect the plasma, this limitation can be accepted. Improvements in the instrument response in the far wings are expected to be enabled by probing the instrument function directly at H_α using a tunable laser, not relying on the interpolation of equation (3). This is an effort of ongoing work.

Note that this limit applies to most W7-X plasmas due to the lack of significant variation of T_i profiles across the W7-X operating range [1]. This causes emission from the same flux surface to have similar Doppler widths across plasmas.

4. Neutral density profiles

Based on the above-introduced framework, radial neutral density profiles can be determined for each LoS available. Three scenarios of electron cyclotron resonance heated are analyzed to assess the obtained neutral density profiles in case of typical W7-X plasmas. An overview of the density and temperature profiles is given in figure 5. The discharges constitute a scan in density with on-axis values of $3.0\times10^{19}\,\mathrm{m}^{-3}$, $4.5\times10^{19}\,\mathrm{m}^{-3}$, and $6.0\times10^{19}\,\mathrm{m}^{-3}$, respectively. Due to a constant heating power of 4.5 MW across all programs, on-axis electron temperatures are found to 5.5 keV, 4.2 keV, and 2.9 keV, respectively. Profiles of the ion temperature are similar with on-axis values around 1.5 keV due to the clamping of the ion temperature in W7-X [1].

Inferred neutral density profiles in case of the high density discharge 20 180920.017 are given in figure 6. Neutral density profiles parameterized by five spline nodes are fitted individually for each available LoS. Due to the varying penetration depths in figure 1, these profiles terminate at the maximal penetration depth of the respective LoS, leaving only a few data

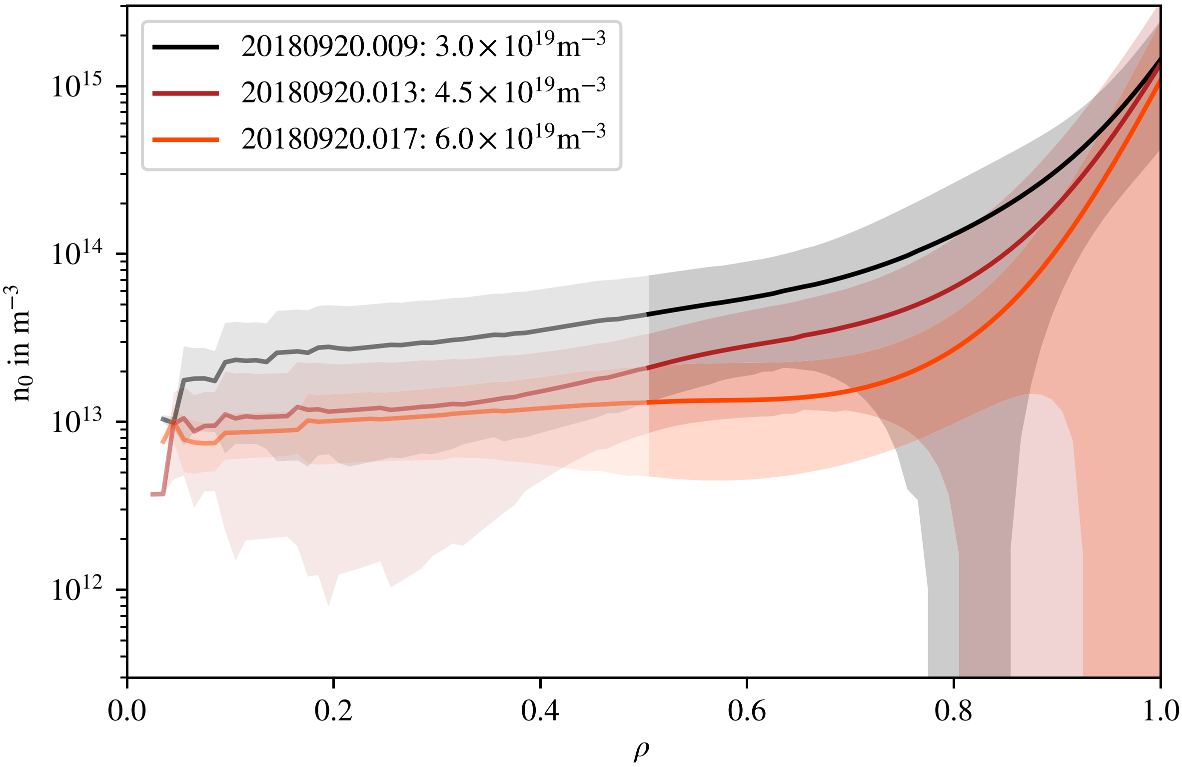

Figure 7. Neutral density profiles in case of plasma discharges 20 180 920.009, .013, and .017, $t = 4.2{-}4.5$ s. The discharges depict a density scan with density increasing with intraday shot number. The region of low sensitivity is grayed out.

points near the magnetic axis. The determined average neutral density profile is given in black; its error is by the shaded region. The error is calculated from the standard deviation of the data at the respective radial locations. Therefore, it is a measure of the spread of neutral density profiles determined from the different lines of sight. Jumps of the average density near the magnetic axis are a numerical artifact caused by averaging a few lines of sight.

In accordance with expectations, the determined average neutral density profile is found to steeply decrease towards the plasma core. The neutral density inside this radius is found to plateau. The scatter between the different lines of sights is up to one order of magnitude across the whole radial coordinate.

In addition to the determined profiles, figure 6(a) depicts two limits the neutral density is expected to fall in between. The upper limit is based on constant neutral pressure with the reference being the outermost value of n_0 at $\rho = 1.2$. The lower limit is obtained by equating the rate of ionization of H^0 with that of recombination of H^+ with free electrons. Both rates are calculated for the local plasma parameters using adf11 coefficients from the OPEN-ADAS [11] data base. This constitutes the limit of no edge sources and no transport. Data points outside $\rho = 1.0$ are not physically meaningful due to the earlier discussed uncertainties in integration paths and plasma profiles.

Figure 6(b) depicts a detailed view of the inferred neutral density profiles resolved by individual LoS. Averages within the individual LoS arrays are given by dashed lines in the respective colors. A systematic deviation between toroidally oriented AEA21_A (purple) and poloidally oriented AEM21 and AET21 (orange, red, and brown) is found to be present in all assessed data sets. Poloidally downwards (AEM21) and poloidally upwards (AET21) directed lines of sight are found to present a good match.

While the absolute magnitude in the region from $\rho = 0.8$ to $\rho = 1.0$ is comparable for the various LoS arrays, the neutral densities predicted by the toroidally oriented lines of sight are systematically lower than the poloidally oriented ones inside $\rho = 0.8$. Due to the strong differences between the viewing geometries within the three-dimensional plasma equilibrium of W7-X, the simplification of a flux surface constant n_0 is expected to cause these systematic deviations. This could hint at asymmetries of neutral density on a flux surface as predicted by modeling [3] and will have to be investigated.

Joint fits assessing different lines of sight imposing a joint neutral density profile were found not to be successful. Following equation (2), the significant variation in neutral density across the different lines of sight of figure 6(b) relates to similar discrepancies in signal amplitude across the lines of sight. The imposed parametrization of the neutral density does not allow for the strong local density variations necessary, rendering a global fit infeasible when following the imposed parametrization of the neutral density.

In order to assess changes in the neutral density population with plasma parameters, figure 7 displays neutral density profiles in case of the density scan of figure 5. A significant variation in n_0 in the outer half of the plasma is apparent while profiles are flat in the inner half. The latter is again assigned to the low sensitivity to emission from this plasma region. In the region of sensitivity, a decrease in neutral density with plasma density is observed. This is consistent with the expectation that more ionization events take place in plasmas of higher collisionality, subsequently decreasing the neutral density.

In addition to this qualitative assessment of the reaction of the neutral density population to an increase in collisionality, the absolute value and radial shape of neutral density profiles obtained with the presented method have been compared to neutral density profiles simulated with the EMC3-Eirene code in previous work by Winters *et al* [3]. Herein, determined neutral densities in the outer half of the plasma were found to lie within the range of poloidal asymmetries predicted by EMC3-Eirene. H_α based neutral densities were found to be lower than simulated values near the magnetic axis, in line with the low sensitivity of the used setup to emission from high-temperature regions.

5. Summary

A framework for the derivation of radial neutral density profiles in W7-X was established and benchmarked against theoretical limits as well as expected scalings with the plasma density. Besides the strong assumption of neutral densities being reducible to a flux surface constant quantity, meaningful neutral density profiles in the outer half of the confined region were obtained. Systematic differences between poloidally and toroidally oriented lines of sight were assigned to the imposed assumptions. A low sensitivity of the method with respect to the neutral density inside half radius was identified. Typical uncertainties are around one order of magnitude.

Neutral densities are found to decrease with increasing plasma density. Besides an expansion of the treatment to a three-dimensional neutral density distribution jointly based on all lines of sight simultaneously, improvements in the edge profile information and the magnetic reconstruction of the associated plasma volumes were named as key points for improvement.

Data availability statement

The data cannot be made publicly available upon publication due to legal restrictions preventing unrestricted public distribution. The data that support the findings of this study are available upon reasonable request from the authors.

Acknowledgments

This work has been carried out within the framework of the EUROfusion Consortium, funded by the European Union via the Euratom Research and Training Programme (Grant Agreement No 101052200—EUROfusion). Views and opinions expressed are however those of the author(s) only and do not necessarily reflect those of the European Union or the European Commission. Neither the European Union nor the European Commission can be held responsible for them.

ORCID iDs

T Romba https://orcid.org/0000-0002-2727-9385
P Zs Poloskei https://orcid.org/0000-0001-7781-5599

References

[1] Beurskens M *et al* (the W7-X team) 2021 *Nucl. Fusion* **61** 116072
[2] Dux R, Cavedon M, Kallenbach A, McDermott R and Vogel G (the ASDEX Upgrade team) 2020 *Nucl. Fusion* **60** 126039
[3] Winters V *et al* (the W7-X team) 2021 *Plasma Phys. Control. Fusion* **63** 045016
[4] Swee C, Geiger B, Dux R, Kumar S, Castillo J, Bader A and Gerard M 2021 *Plasma Phys. Control. Fusion* **64** 015008
[5] Goto M, Sawada K, Fujii K, Hasuo M and Morita S 2011 *Nucl. Fusion* **51** 023005
[6] Fujii K, Atsumi S, Watanabe S, Shikama T, Goto M, Morita S and Hasuo M 2014 *Rev. Sci. Instrum.* **85** 023502
[7] Fujii K, Goto M and Morita S the LHD Experimental Group 2015 *Nucl. Fusion* **55** 063029
[8] Erckmann V *et al* (the W7-AS team and the W7-X teams at IPP Garching, FZK Karlsruhe and IPF Stuttgart) 1997 *17th IEEE/NPSS Symp. Fusion Engineering (Cat. No. 97CH36131)* vol 1 (IEEE) pp 40–48
[9] Grulke O *et al* 2024 *Nucl. Fusion* **64** 112002
[10] Churchill R, Theiler C, Lipschultz B, Dux R, Pütterich T and Viezzer E (the Alcator C-Mod Team and the ASDEX Upgrade team) 2013 *Rev. Sci. Instrum.* **84** 093505
[11] Summers H 2004 (available at: www.adas.ac.uk)
[12] Bozhenkov S *et al* 2017 *J. Instrum.* **12** 10004
[13] Ford O *et al* (the W7-X Team) 2020 *Rev. Sci. Instrum.* **91** 023507
[14] Pavone A *et al* 2019 *J. Instrum.* **14** C10003
[15] Hirshman S, Rij W and Merkel P 1986 *Comput. Phys. Commun.* **43** 143
[16] Jaspers R *et al* 2012 *Rev. Sci. Instrum.* **83** 10D515